High-Power Tunable Terahertz Sources Based on Parametric Processes and Applications

Yujie J. Ding, *Senior Member, IEEE*

(Invited Paper)

***Abstract*—We summarize our progress made on developing widely tunable monochromatic terahertz sources. They have been implemented based on difference-frequency generation (DFG) in GaSe, $ZnGeP_2$, and GaP crystals. Using a GaSe crystal, the output wavelength was tuned continuously in the range of 66.5 to 5664 μm (from 150 to 1.77 cm^{-1}) with the peak power reaching 389 W. Such a high peak power corresponds to a conversion efficiency of $\sim$ 0.1% (a photon conversion efficiency of 19%). A further optimization on the terahertz beam parameter may result in higher output powers and conversion efficiencies. Our experimental results indicate that within the range of 100–250 μm, the output peak powers were higher than 100 W. On the other hand, based on DFG in a $ZnGeP_2$ crystal, the output wavelength was generated to be tunable in the ranges of 83.1–1642 μm and 80.2–1416 μm for two phase-matching configurations. The output power reached 134 W. Using a GaP crystal, the output wavelength was tuned in the range of 71.1–2830 μm, whereas the highest peak power reached 15.6 W. GaP offers an advantage for tuning the output wavelength compared with GaSe and $ZnGeP_2$ since crystal rotation is no longer required. Instead, one just needs to tune the wavelength of one mixing beam within a narrow bandwidth of 15.3 nm. Based on power scaling, a shoebox-sized tunable terahertz source is feasible. We also review our recent results obtained following the investigation of backward DFG and feasibility studies on backward parametric oscillation. The terahertz radiations produced by DFG have pulse durations of about 5 ns, wide tuning ranges, and narrow linewidths, which are quite different from the broadband terahertz pulses. We also describe a few important applications that were realized by taking advantage of the wide tuning range and narrow linewidths of terahertz pulses such as chemical sensing and differentiation of isotopic variants by measuring the rotational spectra of gases and terahertz imaging.**

***Index Terms*— Chemical sensing, difference-frequency generation (DFG), differentiation of isotopic variants, GaP, GaSe, molecular spectroscopy, rotational transitions, terahertz (terahertz) imaging, terahertz parametric oscillation, tunable monochromatic terahertz sources, $ZnGeP_2$.**

I. Introduction

THE REGION of the electromagnetic spectrum with the corresponding frequencies between 0.1 and 10 terahertz has not been completely explored. There are several reasons for us to take advantage of this unique frequency domain. First of all, the transition frequencies between rotational states in gases are within this region [1]. Therefore, it may be feasible to eventually develop a relatively compact rotational spectrometer that can be used to fingerprint molecules. Since the linewidth for the rotational transitions can be 50 MHz (0.0017 cm^{-1}) or narrower for low-pressure gases, such a spectrometer must have a high spectral resolution in order to resolve the spectrum of each rotational transition. Of course, many researchers in the past believe that it is feasible for them to develop the spectrometers working in the domains from visible to mid-infrared for fingerprinting molecules. Unfortunately, most molecules in those domains exhibit the congested and unresolved ro-vibrational spectra [2]. Therefore, it may not be feasible to truly fingerprint molecules in these domains. Secondly, biomedical and biochemical sensing has recently become increasingly important. The water present in the biosamples strongly absorbs terahertz waves. In addition, the scattering of the terahertz waves by the biosamples makes the detection and identification of bioagents difficult. However, when bioparticles become airborne, terahertz waves could still be used to fingerprint the airborne bioparticles. Since almost all the aerosol particles have diameters $\leq$ 10 μm [3], the scattering of the terahertz waves by the bioaerosol particles suspended in the air could be greatly reduced. Thirdly, due to the presence of the atmospheric windows (mainly originated from the absorption dips of the water vapor[1]), terahertz waves could be eventually used for probing as well as for imaging in the ranges of 100 m and farther. There is an additional advantage of utilizing the terahertz waves, i.e., they can penetrate through dust particles. Based on our earlier discussion made above, it is important for us to develop a terahertz system that is capable of taking the multispectral images of targets and simultaneously analyzing the targets based on the terahertz spectra measured by using a tunable and monochromatic terahertz source.

In the past, broadband terahertz pulses were generated based on optical rectifications [4], photoconduction [5], and Cherenkov radiation [6]. All these schemes require ultrafast laser pulses. In order to sense chemicals, time-domain spectroscopy was developed [7]. These broadband pulses were used to measure rotational spectra of gases [8], identify explosives [9], and take terahertz images [10].

In addition to optical rectifications, other parametric processes in nonlinear crystals can be quite efficient for converting optical pulses to the terahertz counterparts. For example, based on terahertz parametric oscillation (TPO) in a $LiNbO_3$ crystal [11], the output peak power of $\sim$milliwatt (a pulse energy of $\sim$10 pJ) was generated under the pump power of 1.2 MW, which corresponds to the conversion efficiency of $\sim 10^{-7}$%. The

Manuscript received October 27, 2006; revised March 4, 2007. This work was supported in part by U.S. Air Force Office of Scientific Research and in part by U.S. Army Research Office.

The author is with the Department of Electrical and Computer Engineering, Lehigh University, Bethlehem, PA 18015 USA (e-mail: yud2@lehigh.edu)

Digital Object Identifier 10.1109/JSTQE.2007.895279

[1]HITRAN database.

threshold intensity was measured to be about 130 MW/cm^2 at 1.064 μm, and the tuning range was measured to be 140–290 μm (1.03–2.14 terahertz). Through injection seeding at $\sim$ 1.07 μm, the highest pulse energy for the terahertz wave was increased to 900 pJ (a peak power >100 mW) for the pump energy of 45 mJ/pulse [12]. Such an output energy corresponds to the conversion efficiency of $\approx 2 \times 10^{-6}$ %.

Recently, by mixing two coherent infrared laser beams in nonlinear optical crystals such as GaSe [13]–[15], $ZnGeP_2$ [16]–[18], and GaP [19], [20], we efficiently generated the terahertz waves with extremely wide tuning ranges and very high peak powers as well as high conversion efficiencies. The widest tuning range achieved by us covers the wavelengths anywhere from 66.5 μm to 5.66 mm (from 4.51 terahertz down to 53 GHz) based on the type-*oe*-*e* phase-matched difference-frequency generation (DFG). On the high-frequency side of the reststrahlen band, we were able to generate the radiation tunable in the range of 2.7–28.7 μm using a different phase-matching configuration [21]. One can see that the tuning range achieved by us almost covers the entire terahertz region (0.1–10 terahertz) and part of the millimeter wave or microwave domain, i.e., 1–5.66 mm (53–300 GHz). Before this result was obtained, such a wide tuning range was only obtained by bulky free-electron lasers. The highest output peak power measured by us is 389 W at 203 μm (1.48 terahertz) and 4.7 W at the wavelength of 1 mm (300 GHz), corresponding to the conversion efficiencies of 0.098% and 0.0012% in terms of the pulse energies, respectively. Another route to a terahertz system is to first develop a current injection coherent terahertz emitter based on semiconductor heterostructures. Since the first report of such an emitter based on GaAs/AlGaAs superlattices [22], significant progress has been made [23]. However, frequency tuning in a wide range could be quite challenging.

We have explored feasibilities of using our widely tunable terahertz sources for certain applications. Indeed, by measuring the absorption spectra of three families of the commonly used chemicals in the vapor phase, we have demonstrated that terahertz absorption spectrometer developed by us could be eventually used to fingerprint molecules [24]. We have also measured the transmission spectra of the CO isotopic variants [25] and biological species [14]. Moreover, we have characterized the Bragg reflectors and 2-D photonic crystals fabricated on the Si wafers [26].

In this paper, we give a comprehensive review of the efficient generation of the widely tunable monochromatic terahertz waves by mixing two near-infrared laser beams with slightly different frequencies in GaSe, $ZnGeP_2$, and GaP crystals. We also summarize the applications realized using widely tunable narrow-linewidth terahertz sources.

II. Power Scaling Using GaSe Crystals

In this section, we summarize our results on scaling up the output powers of the terahertz sources implemented based on DFG using a series of the GaSe crystals with different lengths [13]– [15].

In our experiment, the two mixing beams used for the terahertz and millimeter-wave generation were delivered from the

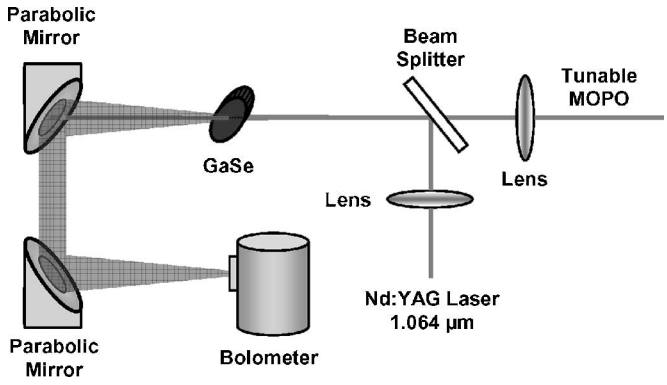

Fig. 1. Experimental setup for observing the phase-matched DFG in a GaSe crystal. The tunable MOPO beam is the idler output from a master oscillator/power oscillator (MOPO) based on two $\beta - BaB_2O_4$ crystals pumped by the third harmonic beam of a Nd:YAG laser at 355 nm.

Nd:YAG laser at 1.0642 μm and the idler output from a master oscillator/power oscillator (MOPO) system pumped by a frequency-tripled Nd:YAG laser beam at 355 nm; see Fig. 1. The Nd:YAG laser and idler beam had pulse durations of 10 and 5 ns, respectively, and both had a repetition rate of 10 Hz. The energies per pulse for the Nd:YAG laser and the idler output were adjustable in the ranges of 9.3 μJ–3.0 mJ and 6.2 μJ–2.0 mJ, respectively. The maximum intensity for the Nd:YAG laser at the nonlinear crystal was $\sim$17 MW/cm^2, whereas that for the idler beam was lower by about a factor of 5. The output energies for the terahertz pulses were detected by a bolometer. Since this bolometer was calibrated by using a pyroelectric joulemeter in the mid-infrared, its responsivities in the terahertz region were as accurate as that for the pyroelectric joulemeter.

One of the most important criterions for us to choose a nonlinear crystal is its absorption coefficient. In fact, it can be readily shown that a figure of merit for the efficient conversion from two optical mixing waves to a terahertz output based on DFG is given by $d_{\text{eff}}^2/(n^3\alpha^2)$, where d_{eff} is the effective nonlinear coefficient, n is the index of refraction, and α is the absorption coefficient at the terahertz frequency. One can see from Fig. 2 that GaSe has the lowest absorption coefficient in the terahertz and millimeter-wave regions among all the inorganic nonlinear crystals [27]. Furthermore, a GaSe crystal has a large second-order nonlinear coefficient. As a result, at 200 μm, the figure of merit for GaSe is five orders of magnitude larger than that for bulk $LiNbO_3$, which is one of the classical materials for terahertz generation. GaSe is a negative uniaxial crystal having a point group of $\bar{6}\,2\,m$. It is worth noting that since it is transparent in the range of 0.62–20 μm, it can be pumped at a variety of the different wavelengths. Since GaSe has a layered structure, the input and output facets are always normal to the optic axis.

For the efficient conversion from the two infrared waves to the terahertz and millimeter waves, two conditions must be satisfied, i.e., the conservations of the total photon energy and the total momentum (phase matching). The first condition is satisfied if the output frequency is the difference of the two optical frequencies. The second one, however, requires the nonlinear optical crystal to possess a sufficiently large amount of the birefringence. In other words, for a given amount of the birefringence

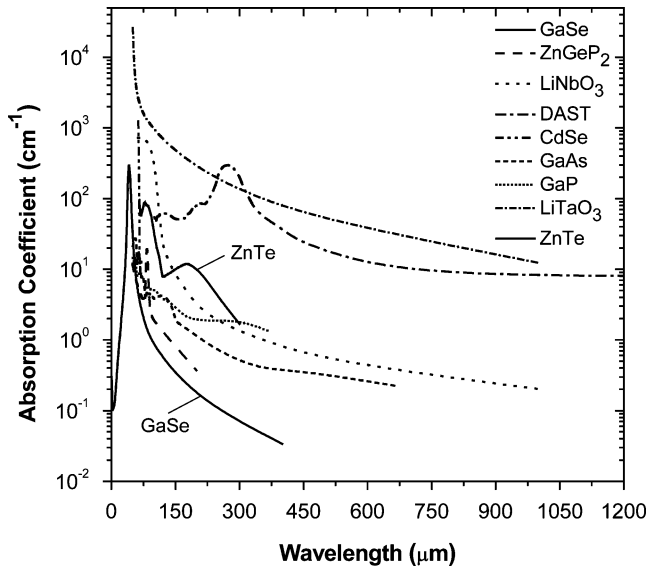

Fig. 2. Absorption coefficients versus wavelength for several nonlinear crystals, some of which were frequently used for terahertz generation. The absorption spectrum for CdSe available covers a narrow wavelength range of 63–71 μm (i.e., a nearly vertical line that almost joins the spectrum for $LiTaO_3$).

available from a specific crystal only a particular output frequency may simultaneously satisfy these two conditions. The polarization for the terahertz or millimeter wave is the same as that of the nonlinear polarization generated by mixing the two pump beams through a second-order nonlinearity. In our experiments, we have used a series of GaSe crystals with the lengths of 4 [13], 7 [13], 15 [13], 20 [14], and 47 mm [15]. As a result, the tuning range was steadily improved from 56.8–810 [13] to 56.8–944 [13], 56.8–1618 [13], 58.2–3540 [14], and 66.5–5664 μm [15], respectively. On the other hand, the highest peak power was significantly scaled up in a sequence of 10.5, 17.0, 69.4, 209, and 389 W. One can see that by using the 47-mm-long GaSe crystal, the tuning range from 53 GHz to 4.51 terahertz (66.5–5664 μm) almost covers the entire terahertz region (0.1–10 terahertz) and part of the millimeter wave or microwave domain, i.e., 1 to 5.66 mm (53–300 GHz); see Fig. 3. In order to achieve phase-matching, the 1.0642-μm pump beam and idler beam from the MOPO system were ordinary and extraordinary waves (designated by o and e) whereas the terahertz and microwave or millimeter wave were extraordinary waves (denoted by e). The pump and output wavelengths were verified by an infrared spectrometer and a scanning etalon consisting of a pair of the parallel Ge plates [13], [14], respectively. The output wavelengths were consistent with those calculated based on DFG.

In addition to the tuning ranges, the output peak powers are important for almost all applications, especially imaging, remote sensing, and communications through atmosphere. The terahertz beams generated by us had a pulse duration measured to be around 5 ns [28] and a repetition rate of 10 Hz. After measuring their pulse energies by using the calibrated bolometer, the peak output powers were determined [see Fig. 4(a)]. The highest output peak power was measured to be 389 W at 203 μm (1.48 terahertz) and 4.7 W at the wavelength of 1 mm (300 GHz) for a pulse energy of $\sim$2 mJ for the idler beam in

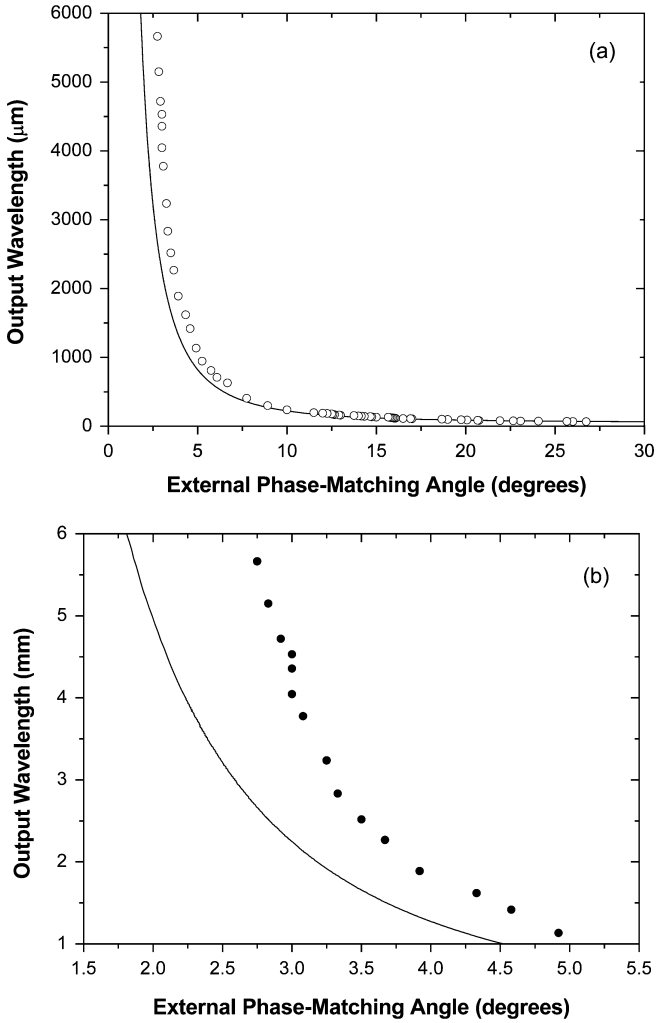

Fig. 3. Output wavelength versus external phase-matching angle for the type-*oe-e* phase-matching interaction in (a) the entire tuning range and (b) the millimeter wave region. Solid curves correspond to the calculation made by us using the phase-matching conditions and dispersion relations for GaSe [29].

the 47-mm-long crystal [see Fig. 4(b)] corresponding to the conversion efficiencies of 0.098% and 0.0012%, respectively. It is worth noting that at the output peak power of 389 W, a tightly focused terahertz beam has a peak intensity of $\sim$1.2 MW/cm^2, which may be sufficiently high for investigating the nonlinear interactions between intense terahertz pulses and certain media. On the other hand, if the terahertz output power is reduced to 1 W (i.e., a pulse energy of 5 nJ) at 200 μm, the required pump energy is $\sim$120 μJ per pulse for each mixing beam. Therefore, a rather compact source can be constructed for generating high peak powers. Fig. 5 illustrates our result of the power scaling for the terahertz source implemented by us using the five different GaSe crystals. One can clearly see that the output powers from four crystals should be much higher after further optimizations according to the linear scaling of the output power with the crystal length. Let us assume that for an optimized configuration, the photon conversion efficiency is close to $\sim$100%. In order to convert the optical pulses at 1 μm to the terahertz counterparts at 200 μm with the terahertz peak power as high as 1 kW, the corresponding pump power should be at least 200 kW.

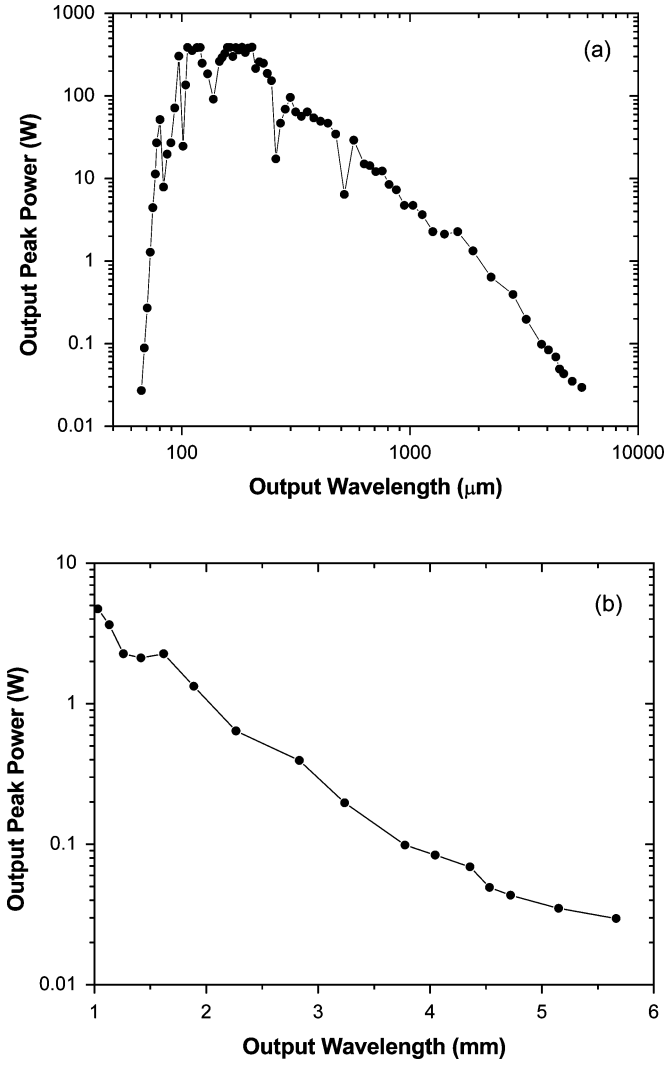

Fig. 4. Output peak power versus output wavelength for phase-matched DFG within (a) the entire tuning range and (b) the millimeter wave region.

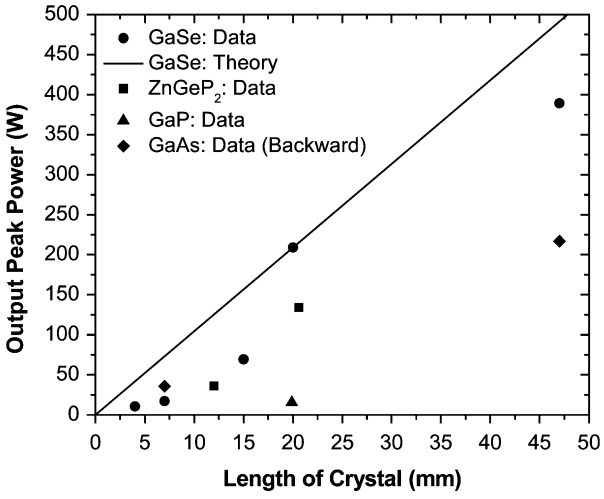

Fig. 5. Output peak powers generated from GaSe, $ZnGeP_2$, and GaP crystals versus crystal length.

Obviously, there is an advantage of using much longer pump wavelengths. For example, if the pump wavelength is increased to 10 μm, the minimum pump power is reduced to 20 kW.

Since the wavelengths of the millimeter wave output are much longer than that for the terahertz waves, the fluctuation of the idler wavelength generated from the MOPO system may significantly affect its power. Assuming that the phase mismatch for the DFG is $\pi/2$ (i.e., the microwave power drops to 81% of the phase-matched value), the deviation of the frequency for the MOPO idler beam is then calculated by using

$$\Delta\nu_i = \frac{c}{4L\left[n_{mm,g}^{(o)} - n_{i,g}^{(o)}\right]} \tag{1}$$

where $n_{\mathrm{mm},g}^{(o)}$ and $n_{\mathrm{i},g}^{(o)}$ are the indices of refraction for the ordinary millimeter wave and idler beam, respectively, and L is the length of the nonlinear medium. For an MOPO, wavelength is $\lambda_i \approx 1.0652$ μm (the millimeter wave wavelength of 1.134 mm) and $L \approx 4.7$ cm, $\Delta\nu_i$ can be estimated to be 5.015 GHz ($0.1672\ \mathrm{cm}^{-1}$). On the other hand, the fluctuation of the incident angle for the pump and idler beams may cause the significant decrease of the microwave power. If the phase mismatch for the DFG is $\pi/2$ due to the deviation of the incident angle from the phase-matched value $[\theta_{\mathrm{ext}}^{(\mathrm{PM})}]$, the angle deviation is shown to be

$$\Delta\theta_{\mathrm{ext}} = \frac{\lambda_i n_i^{(o)}\left[n_i^{(e)}\right]^2}{4L\left\{\left[n_i^{(o)}\right]^2 - \left[n_i^{(e)}\right]^2\right\}\theta_{\mathrm{ext}}^{(\mathrm{PM})}}. \tag{2}$$

For $\lambda_i \approx 1.0652$ μm, $\theta_{\mathrm{ext}}^{(\mathrm{PM})} \approx 4.92^\circ$. Based on (2) $\Delta\theta_{\mathrm{ext}}$ is estimated to be 0.035°. Obviously, the diffraction angle for the idler beam must be smaller than this value. On the other hand, in order to achieve the optimum conversion efficiency, the confocal beam parameter for the millimeter wave should be about half the crystal length. Therefore, the diffraction angle for the MOPO beam should be given by

$$\theta_{\mathrm{diff}} \approx \sqrt{\frac{\lambda_i^2 n_{\mathrm{mm}}^{(o)}}{\pi\lambda_{\mathrm{mm}}\left[n_i^{(o)}\right]^2 L}}. \tag{3}$$

For $\lambda_i \approx 1.0652$ μm and $L \approx 4.7$ cm, we have calculated $\theta_{\mathrm{diff}} \approx 0.003044^\circ$. We can then estimate the beam radius for the idler wave from the MOPO system to be 2.283 mm. All these important issues must be taken into consideration in order to optimize the conversion efficiency from the optical beams to the millimeter or microwave radiation. On the other hand, for the generation of the terahertz waves, these issues are much less important.

III. $ZnGeP_2$ Crystals for Efficient Terahertz Conversion

In this section, we review our recent results on the efficient terahertz conversion by using the $ZnGeP_2$ crystals [16]–[18].

We chose $ZnGeP_2$ for the terahertz conversion, since its absorption coefficients in the terahertz domain are next to the lowest (GaSe) among many frequently used nonlinear crystals

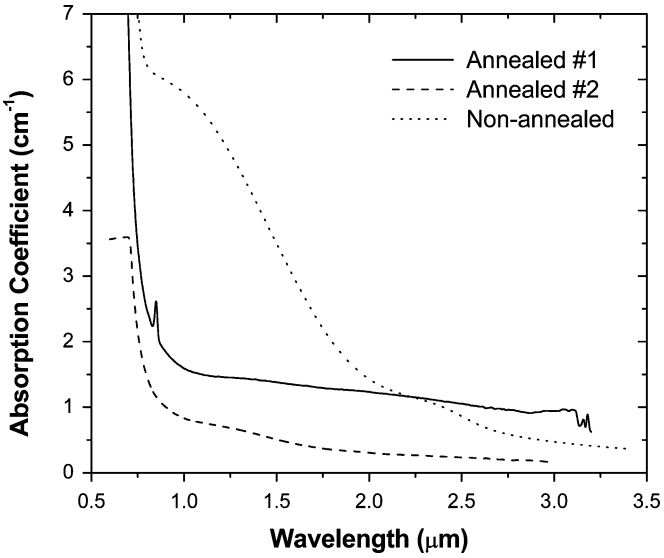

Fig. 6. Absorption spectra for three types of $ZnGeP_2$ crystals.

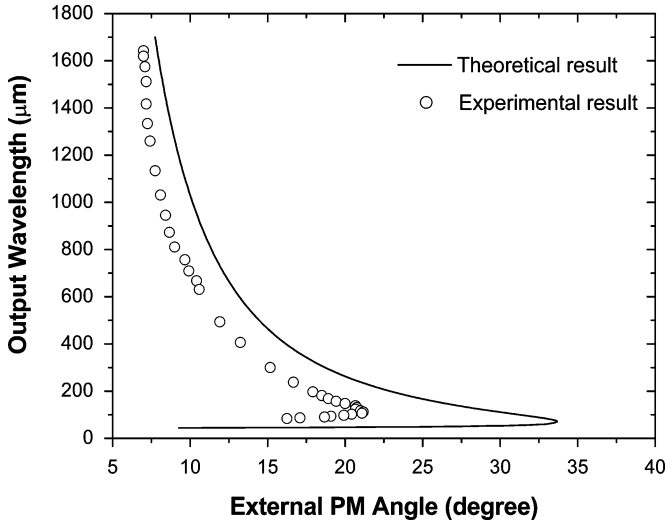

Fig. 7. Collinear phase-matched DFG for *oe-e* configuration in a $ZnGeP_2$ crystal: terahertz output wavelength versus external phase-matching angle. Open circles indicate data; solid lines indicate theory.

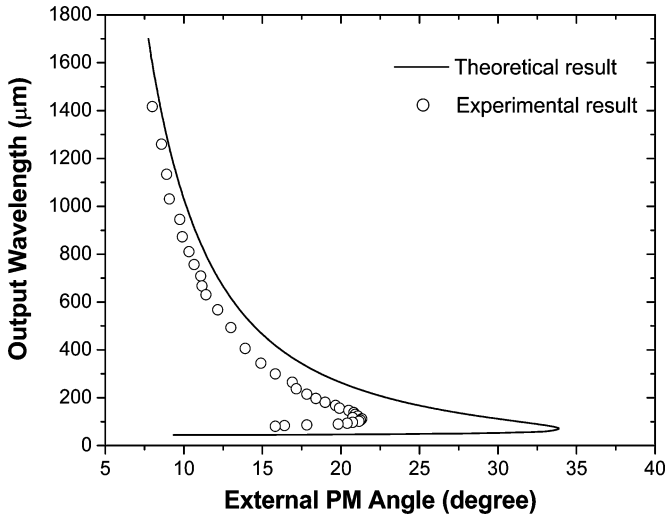

Fig. 8. Collinear phase-matched DFG for *oe-o* configuration in a $ZnGeP_2$ crystal: terahertz output wavelength versus external phase-matching angle. Open circles indicate data; solid lines indicate theory.

[27]. Indeed, according to Fig. 2, the absorption coefficient for $ZnGeP_2$ at 200 μm is about 0.37 cm^{-1}. In comparison, for GaSe, the absorption coefficient is about 0.14 cm^{-1} at the same wavelength. However, it is about 3 cm^{-1} for $LiNbO_3$. $ZnGeP_2$ is a positive uniaxial crystal with a point group of $\overline{4}\,2m$. It possesses a large second-order nonlinear coefficient (d_{36} = 74 pm/V) and figure of merit ($d_{\text{eff}}^2/n^3\alpha^2$). Although it has a transparency range from 0.74 to 12 μm, a $ZnGeP_2$ crystal always has anomalously large absorption coefficients in the near-infrared domain (1–2 μm) that are highly process-dependent (see Fig. 6) [29], [30]. Recently, it was demonstrated that after annealing a $ZnGeP_2$ crystal, its absorption coefficients were dramatically reduced in this wavelength region. In our experiments, we used a 0°-cut $ZnGeP_2$ crystal, which was 20.6 mm long along c-axis and had a cross-sectional area of 15 mm × 14 mm. The absorption coefficient of this $ZnGeP_2$ crystal was measured to be about 0.75 cm^{-1} at 1.064 μm (i.e., annealed crystal #2 in Fig. 6). This is much lower than that used in our prior work [17] and a commonly available crystal (i.e., nonannealed in Fig. 6) [27].

Using 1.064 μm as one of the pump wavelengths, only the configurations of *oe-e* and *oe-o* can be phase-matched in a $ZnGeP_2$ crystal where the first and second letters designate the polarizations for the 1.064 μm and second (idler) pump beams while the third letter corresponds to the polarization for the terahertz beam, respectively [18]. For the two configurations mentioned above, the respective effective nonlinear coefficients depend on the phase matching and azimuth angles (θ, φ)

$$d_{\text{eff}}^{(oe-e)} = d_{36}\sin 2\theta\,\cos 2\varphi; \qquad d_{\text{eff}}^{(oe-o)} = d_{36}\sin\theta\sin 2\varphi \tag{4}$$

where $d_{36} \approx 75$ pm/V [30]. Obviously $d_{\text{eff}}^{(oe-e)}$ and $d_{\text{eff}}^{(oe-o)}$ reach the optimized values at $\varphi = 0°$ and $\varphi = 45°$, respectively. As a result, by properly choosing the value of φ through crystal rotation, we have accessed both configurations. Moreover, the larger the angle θ, the larger are the effective nonlinear coefficients. For the same angle θ, however, $d_{\text{eff}}^{(oe-o)} < d_{\text{eff}}^{(oe-e)}$.

We first measured the angle tuning characteristics for the *oe-e* DFG, as shown in Fig. 7. We have compared our calculations by using three different Sellmeier equations from [31]–[33]. (In [31], however, only the dispersion relation for the ordinary wave is available.) It turns out that the theoretical results based on the Sellmeier equations [32] produced the best fit to our experimental results. For each data point in Fig. 7, a phase-matching peak was achieved by optimizing the terahertz pulse energy through varying θ and one of the pump wavelengths. As a result, tunable and coherent output wavelengths in the range of 83.1–1642 μm (3.61–0.18 terahertz), as shown in Fig. 7, were achieved. On the other hand, Fig. 8 illustrated our results for the *oe-o* configuration. In this case, tunable and coherent terahertz

radiation in the range of 80.2–1416 μm (3.74–0.21 terahertz) was produced. The tuning ranges achieved in Figs. 7 and 8 are much wider than those using the annealed crystal #1 [17]. On the long-wavelength side, the *oe-e* configuration resulted in the longer cutoff wavelength due to the dependence of the effective nonlinear coefficients on θ. Indeed, since $d_{\text{eff}}^{(oe-e)}$ is proportional to $\sin 2\theta$, it is larger than $d_{\text{eff}}^{(oe-o)}$ for the same value of θ [see (4)]. On the other hand, on the short-wavelength side, the cutoff wavelength for the *oe-o* configuration is shorter. This is primarily due to the fact that the absorption for the ordinary wave in the *oe-o* configuration is lower than that for the *oe-e* configuration near 80 μm [27]. The theoretical and experimental phase-matching curves significantly deviated from each other for the two wavelength ranges. These discrepancies could be reduced by modifying the Sellmeier equations for the nonannealed $ZnGeP_2$ crystal [32]. Since the phase-matching angles primarily depend on the index dispersions, especially for the terahertz generation, the phase-matching angles were significantly modified after annealing the crystal. On the other hand, since the wavelength for the terahertz wave is too long, the dispersion in this domain has almost no effect on the phase-matching angles. Based on Figs. 7 and 8, it is obvious that an annealed $ZnGeP_2$ crystal is more advantageous than the conventional one. This is due to the fact that since the range of the measured phase-matching angles is much narrower, it is much easier for us to access the achieved wide terahertz range through the crystal rotation, especially around 100 μm.

For the pump intensity less than 20 MW/cm^2, there is no surface damage for the annealed $ZnGeP_2$ crystal. Therefore, under a pump intensity of 17 MW/cm^2 for the Nd:YAG laser and a pump energy of 2.5 mJ for the MOPO system, the output peak powers at different output wavelengths were measured for the two configurations; see Fig. 9. The measured terahertz radiation had the pulse duration of 5 ns and a repetition rate of 10 Hz. The highest output peak powers for the terahertz were 133.8 W at 237 μm (1.27 terahertz) and 90 W at 196 μm (1.53 terahertz) for the *oe-e* and *oe-o* configurations, respectively. These peak powers are much higher than what we obtained for the annealed crystal #1 [17]. However, they are lower than those generated from the GaSe crystal with the same length; see Fig. 5. The peak power for the *oe-e* configuration was much higher than that for the *oe-o* configuration since $d_{\text{eff}}^{(oe-e)}$ is larger than $d_{\text{eff}}^{(oe-o)}$ [see (4)]. Therefore, the *oe-e* configuration offers an advantage over the *oe-o* configuration in terms of the peak power. In addition, the *oe-o* configuration produced longer wavelengths. On the other hand, the *oe-o* configuration offers an advantage of generating shorter wavelengths. In our experiments, we have consistently observed two dips near 110 μm (see Fig. 9), which are consistent with the previously result [27]. Using an expression for the conversion efficiency [18], the conversion efficiencies were calculated to be 0.048% and 0.039% for the *oe-e* and *oe-o* configurations, respectively, which are in good agreements with our experimental results. In order to make the terahertz source much more compact, we can introduce intracavity DFG, i.e., placing a $ZnGeP_2$ crystal inside a cavity for an optical parametric oscillator (OPO). One can use an Er-doped fiber laser at the wavelength of 1.55 μm as a pump source to achieve an OPO with the signal and idler wavelengths near 3.1 μm.

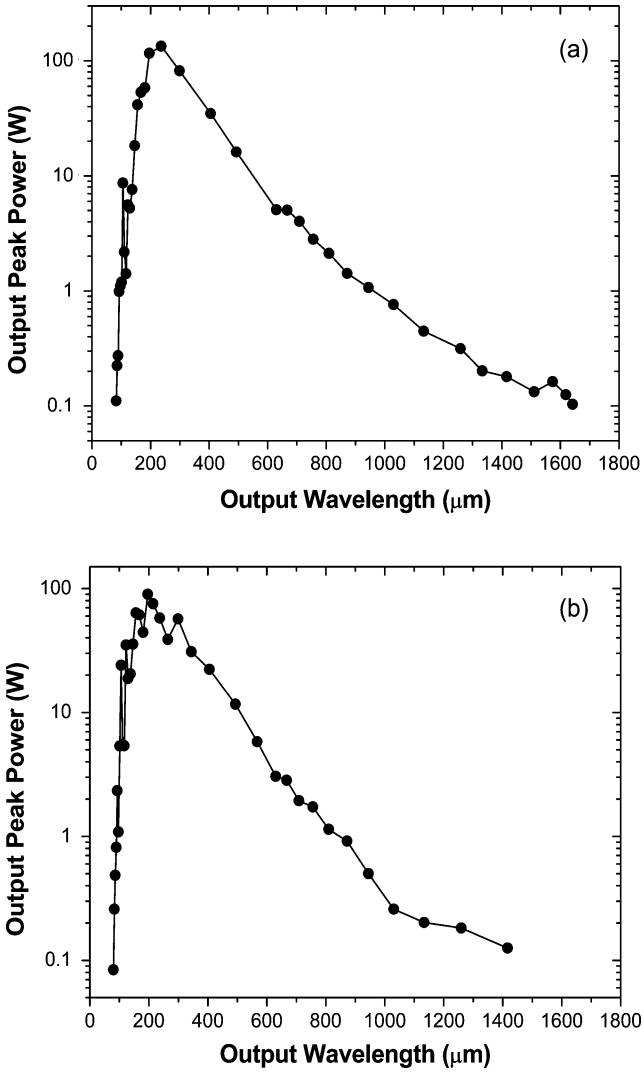

Fig. 9. Output peak power versus output wavelength in a $ZnGeP_2$ crystal. (a) *oe-e* configuration and (b) *oe-o* configuration.

IV. Terahertz Generation From a GaP Crystal

In this section, we summarize our recent results on the efficient generation of terahertz pulses from one of the cubic crystals [19], [20].

As discussed in the previous sections, birefringence for the GaSe and $ZnGeP_2$ crystals was essential for phase-matching the DFG. However, in order to tune the output wavelength in the terahertz region one must rotate these crystals. Although zinc-blende crystals such as GaAs and GaP do not possess any measurable birefringence; phase-matching condition for the terahertz conversion can still be satisfied due to the presence of the reststrahlen bands in the terahertz region [34], [35]. According to our theoretical results [34], [35], GaAs and GaP could be used to generate tunable terahertz beams by tuning the mixing wavelengths in the ranges of 1.247–1.333 μm and 0.9958–1.034 μm, respectively.

A GaP crystal was first used to achieve upconversion, i.e., the generation of a visible output by mixing a visible input with each of the five far-infrared wavelengths resonant to the rest-strahlen band of the crystal [36]. Recently, this crystal was used for generating the tunable terahertz beam based on noncollinear phase-matched DFG [37]. As a result, a tuning range of 40.5–300 μm and a peak power of 100 mW were obtained. Such a tuning range was achieved by changing the angle formed between the propagation directions of the two mixing beams. However, under such a configuration, the spatial overlap between the terahertz beam and the two mixing beams inside the crystal was sacrificed due to the relatively large angles formed among them inside the crystal. Obviously, in order to maximize the spatial overlap among the three parametric beams, a collinear propagation configuration is preferred such that a much wider tuning range and higher output powers for terahertz waves are feasible.

The two infrared laser beams used in our DFG experiment are described in detail in Section II. A GaP crystal with a length of 19.9 mm along the [001] direction and a dimension of 25 mm $\times$ 25 mm for the cross section was used in our DFG experiment. According to Fig. 2, this crystal has reasonably low-absorption coefficients in the terahertz region. It has the cubic structure $(\bar{4}3m)$. If the two mixing wavelengths are close to 1.064 μm, the coherence lengths for the DFG process are still long enough such that the parametric process is regarded as being phase-matched [35]. Indeed, based on the dispersion relation [38], the coherence length is in the range of 0.168–80.7 mm for the terahertz parametric conversion. On the other hand, when the wavelength for the second mixing beam is tuned from 1.04202 to 1.06382 μm (shorter than 1.064 μm), the coherence lengths are also long. Therefore, for all these mixing wavelengths, the DFG process is phase-matched.

Since GaP is an isotropic crystal, the momentum mismatch is independent of the propagation directions and polarizations of the two mixing beams. However, the propagation directions and polarizations affect the effective second-order nonlinear coefficient for the DFG similar to GaAs [39], and therefore, the output power. In our experiment, we chose the parallel and orthogonal polarization states for the two mixing beams: 1) the parallel polarization state, i.e., the two mixing beams were polarized in a plane perpendicular to the [010] axis and 2) the orthogonal one for which the first mixing beam was polarized parallel to the [010] axis. In order to obtain the angle-tuning spectra, we rotated the crystal around an axis being parallel to the [010] direction and going through the point where the two mixing beams entered the crystal. The spectra were measured by us at different wavelengths for the second mixing beam; see Fig. 10(a) and (b). When the external angle was close to 0°, the output powers were not measurable since the effective nonlinear coefficient vanishes. The maximum output powers actually occurred at the optimum angles of about 62° and 53° for the parallel and orthogonal polarizations, respectively. When the wavelength of the second mixing beam was set to values shorter than 1.064 μm, the optimum angles were about the same as those mentioned above. As the incident angle was increased, the effective second-order nonlinear coefficient was also increased. However, beyond the optimum values, some portions of the terahertz beam were ultimately trapped inside the crystal due to the divergence of the terahertz beams.

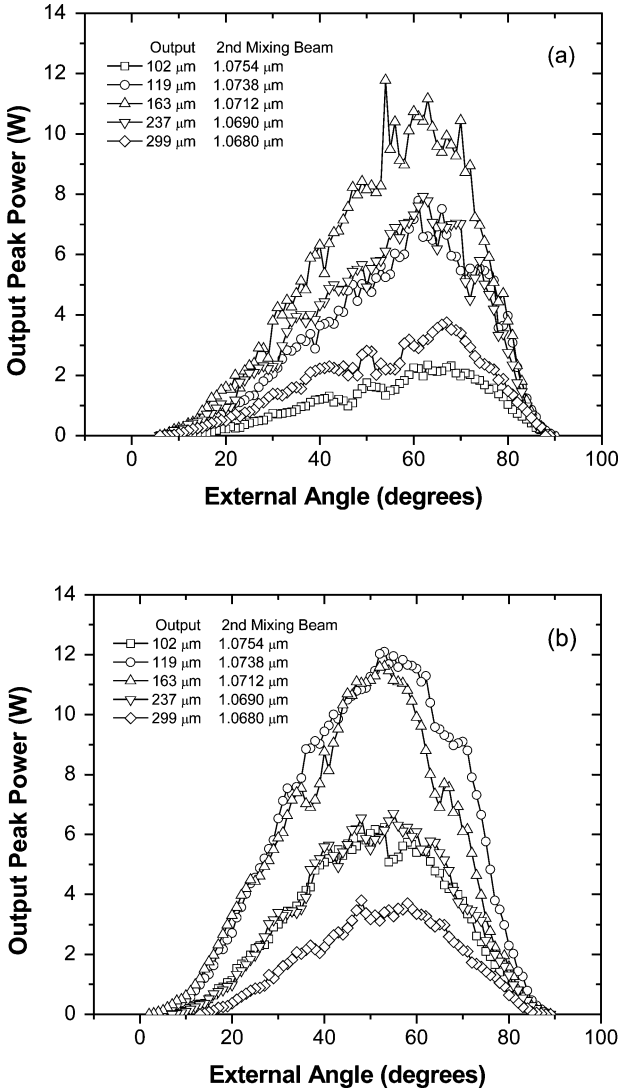

Fig. 10. Angle-tuning spectra. Output peak power versus external angle for several different wavelengths of the second mixing beam, which are longer than 1.064 μm and (a) parallel and (b) orthogonal polarizations.

When the wavelength of the second mixing beam was tuned to those longer than 1.064 μm, the spectrum of the output peak power was measured for the two polarizations with the incident angles set to 62° and 53°, respectively; see Fig. 11. One can see that the tuning ranges of 84–1134 (0.26–3.57 terahertz) and 83–810 μm (0.37–3.61 terahertz) for the parallel and orthogonal polarizations were achieved, respectively. The highest output peak power was measured to be 15.6 W at 173 μm (a conversion efficiency of $\sim$0.002%). Such a peak power is an order of magnitude lower than that of the 2-cm-long GaSe and $ZnGeP_2$ crystals (Fig. 5). One can see several dips appearing in the spectra of Fig. 11, primarily due to the absorption of the water vapor in the air. On the other hand, when the wavelength of the second mixing beam was tuned to those shorter than 1.064 μm, we also generated the widely tunable terahertz waves for the two polarization states (see Fig. 12). For the parallel polarization state,

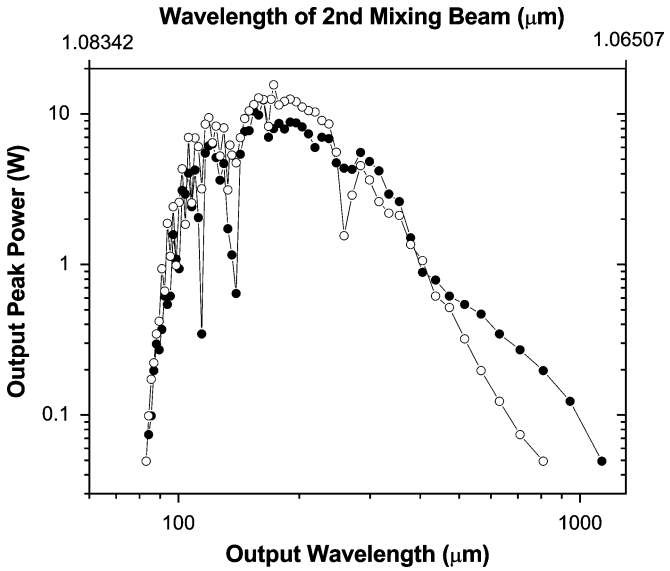

Fig. 11. Output peak power versus output wavelength when the wavelength of the second mixing beam is longer than 1.064 μm. Parallel polarizations (external angle of 62° dots) and orthogonal polarizations (external angle of 53° open circles).

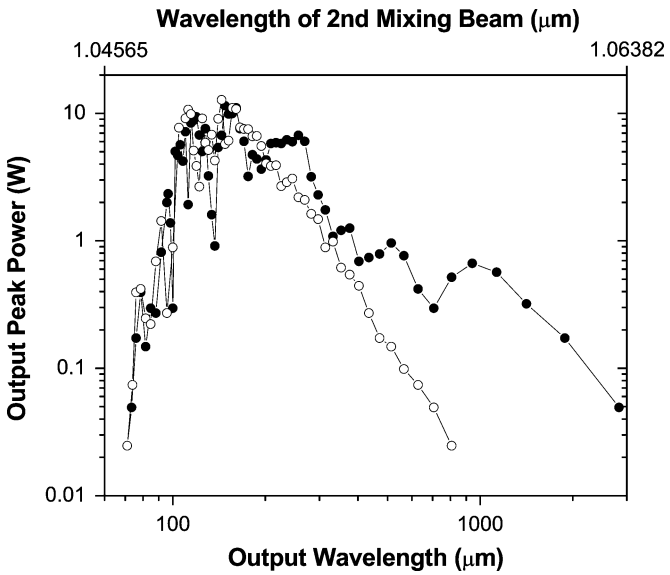

Fig. 12. Output peak power versus output wavelength when the wavelength of the second mixing beam shorter than 1.064 μm. Parallel polarizations (external angle of 62° dots) and orthogonal polarizations (external angle of 53° open circles).

the output wavelengths covered the range from 71.1 to 2830 μm (0.106–4.22 terahertz), i.e., a much wider tuning range compared to the rest of the configurations. Such a tuning range was achieved simply by tuning the wavelength of the second mixing beam in a narrow bandwidth of ~15.3 nm. As a result, beam steering is no longer needed. In addition to the large difference in the tuning ranges, the two polarizations for the wavelengths of the second mixing beam shorter than 1.064 μm yielded the shorter cutoff wavelengths.

Compared with the previous result [37], we have extended the long wavelength end of the tuning range from 300 to 2830 μm

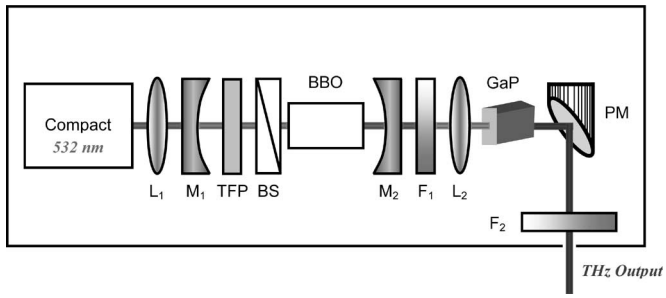

Fig. 13. Design of a shoebox-sized terahertz source.

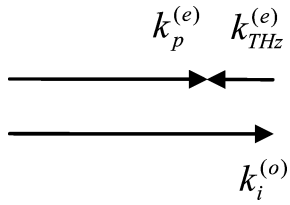

Fig. 14. Wave vectors of the three parametric waves satisfying the phase-matching condition for the configuration of the backward terahertz DFG in a GaSe crystal $k_p^{(e)} - k_i^{(o)} = -k_{\text{terahertz}}^{(e)}$.

and improved the peak power by two orders of magnitude. By using the collinear propagation configuration, we have optimized the spatial overlap among three parametric beams within the 2-cm-long crystal. Therefore, we have taken advantage of the long coherence lengths for the collinear DFG. One can improve the conversion efficiency by using a GaP crystal with the input and output facets parallel to the $(1\,\bar{1}\,0)$ plane [20]. This is due to the fact that for a cubic crystal, the effective nonlinear coefficient has the highest value if the two mixing beams propagate in the direction perpendicular to this plane. Fig. 13 shows our design of a tunable and compact (i.e., a shoebox size) terahertz source. It is expected to produce a peak power up to 100 mW at 200 μm.

V. Backward Terahertz Parametric Processes

In this section, we first summarize our results on the backward DFG achieved by mixing two infrared laser beams in two GaSe crystals [40]. We then review our results on the feasibility study of a backward TPO by using GaSe and $ZnGeP_2$ crystals [41].

Backward OPO [42], corresponding to one of the most fundamental coherent nonlinear processes, has not yet been demonstrated to the best of our knowledge. For such a unique configuration, one of the parametric waves (i.e., the signal) propagates in a direction opposite to that for the pump wave, as shown in Fig. 14. A backward OPO is completely different from the forward OPO (i.e., all the three parametric waves propagates in the same direction) [43]. Since the signal and idler waves counterpropagate in a nonlinear medium, an oscillation can occur without the presence of even a mirror, whereas the forward OPO can never take place without a cavity for one of the parametric waves (i.e., the signal). Moreover, the linewidth for the backward OPO is much narrower than that for the forward one [43]. Furthermore, due to severe temporal walkoff, the backward OPO would not be efficient for producing ultrafast pulses. However, owing

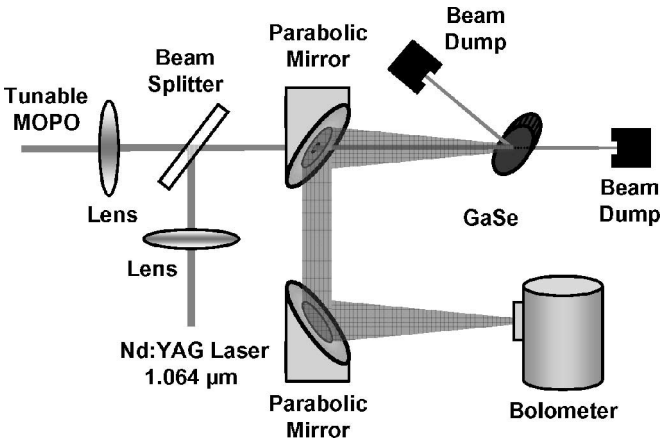

Fig. 15. Experimental setup for observing the phase-matched backward DFG in a GaSe crystal.

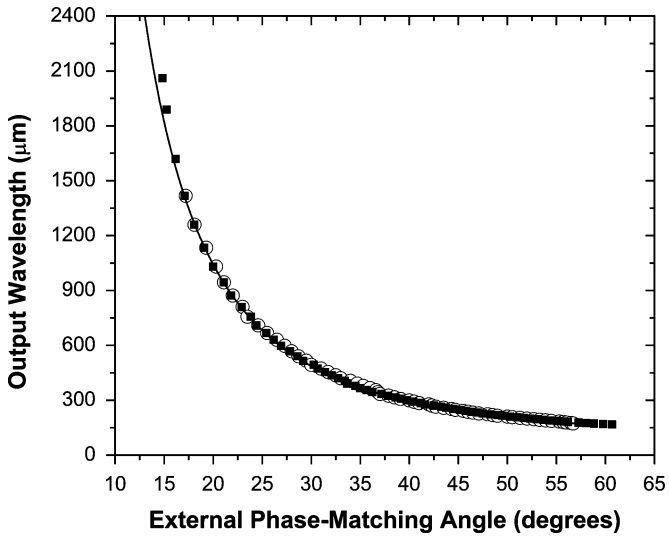

Fig. 16. Angle-tuning characteristics for the type-*eo-e* backward terahertz DFG in two GaSe crystals. The open circles and filled squares correspond to our experimental results for crystals #1 and #2, respectively, whereas the solid curve was obtained by using the phase-matching condition and the dispersion relations [29].

to the fact that one of the parametric waves has its wave vector opposite to those of the other two waves, the phase-matching condition can be satisfied only if the birefringence of a nonlinear optical crystal in the infrared region is anomalously large. In addition to such a stringent requirement, the nonlinear crystal must be transparent in the wavelength range within which the output wave is produced. As a result, only a few nonlinear optical crystals can satisfy these two conditions. Furthermore, a backward OPO has a threshold that is inherently much higher than that for a forward OPO due to the lack of a cavity. These are the underlying reasons why the birefringence-based backward OPO has not been achieved for the last four decades.

In the past, the backward DFG [44] and parametric fluorescence [45] with the output frequencies in the mid-infrared region were observed in $NaNO_2$. However, since $NaNO_2$ is hygroscopic and the damage threshold is relatively low, it is not possible to achieve the backward OPO in such a crystal. Recently, we made a feasibility study of achieving the backward mid-infrared OPO by using GaSe [46]. However, observing such a process in this crystal is quite challenging since the internal angle required to achieve the backward phase matching in the mid-infrared region is always larger than the critical angle for total internal reflection. Although the quasi-phase-matching in the mid-infrared region is an alternative, the period of the periodically inverted nonlinear domains required to achieve a backward OPO using the first-order nonlinear grating in such a spectral region [47] is still beyond the current fabrication capabilities. On the other hand, it is quite possible to achieve the backward TPO based on quasi-phase-matching [48]. However, almost all the periodically poled ferroelectric crystals such as $LiNbO_3$ possess relatively large absorption in the terahertz region. Therefore, the threshold intensities are either too close to or sometimes even higher than the damage thresholds due to the relatively short propagation distances for the parametric waves, dictated by the large absorption coefficients for the terahertz waves.

For the backward DFG experiment, the Nd:YAG laser and MOPO idler beams were focused onto each GaSe crystal with the average beam radii approximately 300 μm and 1 mm, respectively. The two GaSe crystals used in our DFG experiment were 7 and 47 mm long along their respective optic axes (crystals #1 and #2) with the cross-sectional areas of 35 mm $\times$ 15 mm and 23 mm $\times$ 45 mm, respectively. An off-axis parabolic metallic mirror was placed in front of each GaSe crystal, as shown in Fig. 15. In order to allow the two mixing beams to pass through this mirror, we drilled a small hole with the diameter of about 1.5 mm through the mirror. Since the propagation direction of the backward terahertz beam is not parallel to that of the two mixing beams outside each GaSe crystal due to the difference in their indices of refraction and the backward terahertz beam diffracts much faster as it propagates, the loss of the backward terahertz wave that leaked through the small hole is negligible. The generated backward-propagating terahertz wave was collimated by one off-axis parabolic metallic mirror and then focused onto a Si bolometer by the second mirror, as shown in Fig. 15.

For the type-*eo-e* backward DFG, we measured the angle tuning curves in the two GaSe crystals by using a Si bolometer; see Fig. 16. The generated frequencies in the terahertz region were verified by scanning a homemade etalon consisting of a pair of the parallel Ge plates. According to Fig. 16, the wavelength of the backward-propagating wave was tuned in a range of 172.7–1416.7 (0.212–1.74) and 167.6–2060 μm (0.146–1.79 terahertz) for crystals #1 and #2, respectively. Apparently, the measured tuning curves are in an excellent agreement with the calculated one; see Fig. 16. Since the output pulse energies produced by crystal #2 are much higher, the two limiting wavelengths (defining the tuning range) at which the output pulse energies can be still measured by the bolometer are shifted toward the shorter and longer values, respectively. As a result, the tuning range for crystal #2 is much wider.

The output pulse energies were measured by using the calibrated Si bolometer after a proper attenuation. Using the pulsewidth $\sim$5 ns for the terahertz waves measured by us based

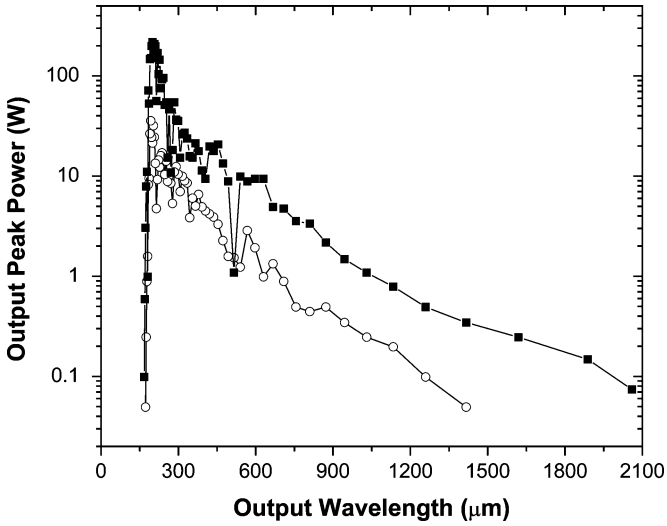

Fig. 17. Output peak power versus the output wavelength measured for the type *eo-e* phase-matched backward DFG in the two GaSe crystals: crystal #1 (open circles) and crystal #2 (filled squares).

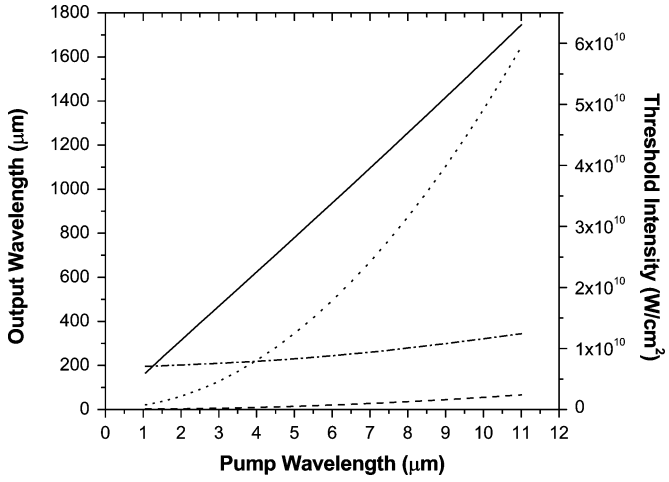

Fig. 18. Output wavelength versus the pump wavelength (solid line) for the *e-oe* configuration is plotted when the total internal reflection angle for the terahertz waves generated based on the backward TPO is equal to the phase-matching angle. The corresponding threshold intensity is also plotted versus pump wavelength for different lengths of a GaSe crystal: 1 cm (dotted line) and 5 cm (dashed line). The dash-dotted line corresponds to the optimum output wavelength at which the threshold power reaches a minimum value for each pump wavelength.

on the terahertz frequency upconversion [28], we then determined and plotted the output peak powers versus the output wavelength for the two GaSe crystals in Fig. 17. A sudden drop in the output power at the short-wavelength side was due to the existence of a critical angle (measured to be ≈18°) above which the total internal reflection for the terahertz wave took place inside each of the GaSe crystals. Such a critical angle can be calculated from

$$\theta_{\rm cr} = \theta_{\rm PM} = \sin^{-1}\left\{\left[n^{(e)}_{\rm terahertz}\left(\theta_{\rm PM}\right)\right]^{-1}\right\} \qquad (5)$$

where $\theta_{\rm PM}$ is the phase-matching angle for the backward *eo-e* DFG. The critical angle calculated using (5) is in very good agreement with the measured value. In comparison, there was no critical angle for the forward DFG in any GaSe crystal; see Section II. The highest output peak power generated from crystals #1 and #2 was 35.7 W at 193 μm and 217 W at 199.8 μm, which corresponded to the conversion efficiencies of 0.0051% and 0.031%, respectively, in terms of the powers from the MOPO idler beam to the terahertz output. Compared with the forward configuration, the peak power from the 7-mm-long crystal was higher, whereas that from the 47-mm-long crystal was much lower; see Fig. 5. Using $w_p \approx 300$ μm and $w_i \approx 1$ mm (the beam radii for the pump and idler beams), the highest output peak power was calculated to be 62 and 410 W for crystals #1 and #2, corresponding to the power conversion efficiency of 0.0088% and 0.059%, respectively [40]. These values were in the same orders of magnitude as the measured ones. When the crystal length was increased from 7 to 47 mm, the highest peak power for the terahertz wave was increased by a factor of 6.1 due to linear power scaling.

The highest output power generated in our experiment can be further scaled up. First of all, by optimizing the confocal parameter for the terahertz wave, the output power may be significantly increased. Secondly, for the photon conversion efficiency of ≈100% with the same mixing wavelengths as those used in our experiment, the output peak power can be as high as several kilowatts. On the other hand, by using a wavelength much longer than 1 μm in order to avoid two-photon absorption [49], the output peak power can be readily increased to 100 kW by using higher pump intensities in a 5-cm-long crystal. Such a peak power corresponds to a peak intensity of higher than 65 MW/cm^2 after tightly focusing the terahertz beam.

In Fig. 18, we have plotted the output wavelength versus the pump wavelength under a critical condition (5). Due to the presence of the absorption for the terahertz waves, the corresponding threshold intensity required to achieve the backward TPO can be calculated by using the following formula [41], [42]:

$$I_{\rm th}\left(\alpha\right) = \frac{\left(4y\right)^2 + \left(\alpha L\right)^2}{4\pi^2} I_{\rm th} \qquad (6)$$

where α is the absorption coefficient for the terahertz wave, $I_{\rm th}$ is the threshold intensity if α = 0, and y is determined by $4y = -(\alpha L)\tan(y)$. Based on (6), we have calculated the threshold intensities after taking into consideration the absorption for the terahertz waves [27] and presented our results in Fig. 18. For each pump wavelength, one can determine the threshold power by using $P_{\rm th} = I_{\rm th}(\alpha)\pi w_{\rm p}^2$. For the optimum focusing condition for a Gaussian beam [50], one obtains the optimum output wavelength at which $P_{\rm th}$ reaches a minimum value; see Fig. 18. For example, at $\lambda_p \approx 1.86$ μm, the optimum value for $\lambda_{\rm terahertz}$ is ≈ 211 μm for $L \approx 5$ cm. Since the bandgap energy for GaSe is about 2 eV, at the pump wavelength of 1.86 μm, one can completely eliminate two-photon and three-photon absorption. According to Fig. 18, at $\lambda_p \approx 1.86$ μm the threshold intensity is calculated to be 116 MW/cm^2 for a 5-cm-long GaSe crystal at the critical output wavelength of 292 μm. This wavelength is quite close to the optimum value (i.e., 211 μm). When the crystal length is reduced to 1 cm, however, the

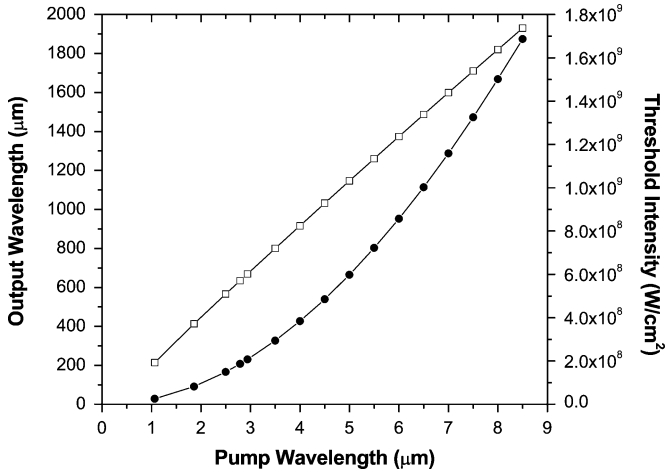

Fig. 19. Signal wavelength (open squares) and threshold intensity (filled dots), corresponding to the minimum threshold power, see the text, are plotted versus the pump wavelength for the backward TPO with the *o-ee* configuration in a 5-cm-long $ZnGeP_2$ crystal.

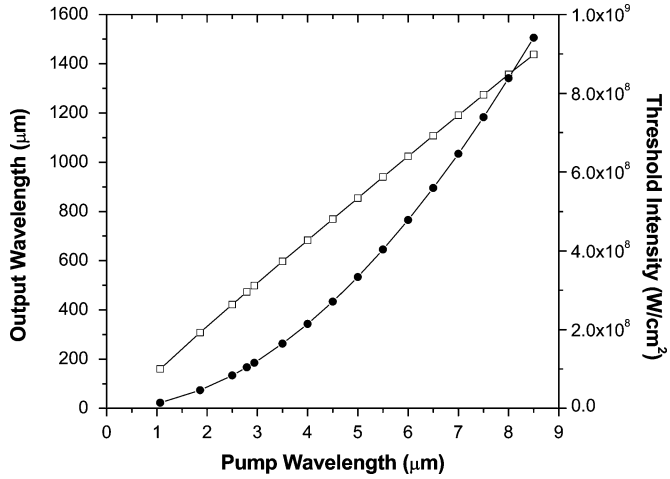

Fig. 20. Optimum output wavelength (open squares) and the corresponding threshold intensity (filled dots) versus the pump wavelength for the backward TPO with the *o-eo* configuration at $\theta = 90^\circ$ in a 5-cm-long $ZnGeP_2$ crystal.

threshold intensity is increased to 2.0 GW/cm^2. Based on [51], these threshold values are much below the damage threshold for this crystal. As the pump wavelength is increased, the critical output wavelength is linearly increased. At 10.6 μm, it is increased to 1679 μm, as shown in Fig. 18. This value is much longer than the optimum value (i.e., 403 μm). Consequently, the threshold intensity at such a critical wavelength is significantly increased due to the wavelength scaling. Indeed, for $L \approx$ 5 cm, the threshold intensity is calculated as 2.3 GW/cm^2. Based on [52], such a value is still below the damage threshold for the CO_2 laser pulses. Compared with the thresholds at the pump wavelength of 1.86 μm, there is no advantage of using 10.6 μm as a pump wavelength in order to observe the backward TPO since the maximum conversion efficiencies are more or less the same for the two pump wavelengths [i.e., the dependence of the critical output wavelength on the pump wavelength is linear (Fig. 18)].

In addition to the GaSe crystal, a $ZnGeP_2$ crystal can also be used to observe the backward TPO. A pump wavelength should be in the range of 2.5–8.5 μm in order to reduce the absorption coefficients down to $<$0.1 cm^{-1} [29]. On the other hand, in the terahertz region, the absorption coefficients for the $ZnGeP_2$ crystal are higher than those for the GaSe crystal (see Fig. 2). Since the bandgap energy for this crystal is also 2 eV, in principle, one can avoid two-photon and three-photon absorption as long as the pump wavelength is longer than 1.86 μm. The phase-matching condition can be satisfied for the two configurations

$$k_p^{(o)} = k_i^{(e)} - k_{\text{terahertz}}^{(e)} \qquad (\text{for } o - ee) \tag{7}$$

$$k_p^{(o)} = k_i^{(e)} - k_{\text{terahertz}}^{(o)} \qquad (\text{for } o - eo). \tag{8}$$

The respective nonlinear coefficients are given by (4). For the *o-ee* configuration, we have minimized the threshold power according to $P_{\text{th}} = I_{\text{th}}(\alpha)\pi w_{\text{p}}^2$ for the optimum focusing case, where the absorption coefficients were taken from [27] in the same way as that for the GaSe crystal mentioned earlier. In Fig. 19, we have plotted the optimum output wavelength and the corresponding threshold intensity versus the pump wavelength for such a phase-matching configuration with the length of the $ZnGeP_2$ crystal $L \approx 5$ cm. One can see from Fig. 19 that the threshold intensities are in the range of 2.6×10^7–1.7×10^9 W/cm^2. According to [53], these values are certainly below the damage thresholds for a high-quality $ZnGeP_2$ crystal.

On the other hand, for the *o-eo* phase-matching configuration, the minimum threshold powers occur at the phase-matching angle of $\theta = 90^\circ$. At such an angle and for the length of the crystal $L \approx 5$ cm, we have plotted the output wavelength and the corresponding threshold intensity versus the pump wavelength in Fig. 20. When the pump wavelength is increased from 2.5 to 8.5 μm, the threshold intensity is increased from 8.4×10^7 to 9.4×10^8 W/cm^2. Compared to the *o-ee* configuration, the threshold intensities for the *o-eo* configuration are significantly lower. This is due to the fact that the effective nonlinear coefficients for the *o-eo* configuration are higher at $\theta = 90^\circ$ [see (4)]. Furthermore, the *o-eo* configuration offers the higher values of the maximum conversion efficiencies (i.e., those when the photon conversion efficiencies are close to 100%).

VI. Applications of Using Tunable Narrowband Terahertz Pulses

In this section, we highlight the applications realized so far by using the tunable narrow-linewidth terahertz pulses.

First of all, a widely tunable terahertz source was used to identify chemicals by directly measuring the absorption spectra of gases [24]. This is due to the fact that frequency spacing among rotational energy states of the molecules in the gas phase lies in the range of 30 GHz–3 terahertz (100–10 000 μm, 1–100 cm^{-1}). Therefore, a tunable terahertz or submillimeter source can be used to measure the dipole-allowed transitions between any two rotational energy states. In the past, Fourier-transform infrared (FTIR) spectroscopy [54] was primarily used for the spectroscopic studies of the molecules. However, FTIR requires

an extremely long gas cell [55]. Furthermore, absorption coefficients could not be accurately measured due to the low powers of the FIR sources currently available. On the other hand, terahertz time-domain spectroscopy was used to measure the absorption due to the rotational transitions of the molecules in the vapor phase [8]. However, Fourier transform was always required in order to obtain an absorption spectrum for each chemical species.

The terahertz source used in our experiment was implemented by mixing the two infrared beams at the wavelengths of around 1 μm based on DFG in a GaSe crystal (see Section II). It has a typical linewidth of 0.36 cm^{-1} and a tuning range of 58.2–3540 μm (2.82–172 cm^{-1} or 0.0848–5.15 terahertz). Using such a terahertz source, we have directly measured three members of the alcohol homologues, two members of the ketones homologues, and two members of the alkyl-halogenides homologues [24]. Following our measurements, we concluded that a direct measurement of the absorption spectrum was a simple and effective technique for fingerprinting the chemicals in the vapor phase.

In order to measure the absorption for each type of chemicals in the vapor phase, we used the two identical gas cells each of which was 15 cm long. One cell was filled with the saturated chemical vapor by injecting a sufficient amount of the high-purity chemical in liquid form at a temperature of 23 °C and a pressure of 1 atm. The second cell was filled with high-purity helium gas at the same temperature and pressure, which was used as a reference. By frequency-tuning our terahertz source, we have measured the transmittances for the terahertz wave going through each chemical species in the vapor phase. We have then obtained the absorption spectrum.

We first measured the absorption spectra for three members of the alcohol homologues, i.e., the methanol vapor [CH_3OH, Fig. 21(a)], ethanol vapor [C_2H_5OH, Fig. 21(b)], and isopropanol vapor [C_3H_7OH, Fig. 21(c)]. All the three vapors exhibited completely different transition peaks, although they have similar molecular structures. Among these three spectra, the methanol vapor had the strongest absorption and exhibited many transition peaks, similar to that given in [56]. In particular, the wavelength of 118.8 μm (the wave number of 84.18 cm^{-1} or 2.525 terahertz) [57] was used as a local-oscillator transition line in a Schottky mixer to monitor the hydroxyl radical in the space. On the other hand, the ethanol vapor had a less number of the transition peaks, probably due to the broadening of the individual peaks. The isopropanol vapor had an even less number of the absorption peaks. In addition, the absorption peaks for the isopropanol vapor were weaker than those for the ethanol vapor and much weaker than those for the methanol vapor.

On the other hand, the spectra for the two members of the ketones homologues [i.e., acetone $(CH_3)_2CO$ and butanone C_3H_8CO], having similar molecular structures, were also different; see Fig. 22. The acetone vapor [Fig. 22(a)] exhibited the strongest absorption among all the chemicals measured by us. Both acetone and methyl ethyl ketone vapors exhibited the broadened absorption peaks in the range of 5–40 cm^{-1}, although the apparent peak for the butanone vapor was red-shifted relative to that for the acetone vapor. The absorption coefficients for the butanone vapor were much lower than those for the acetone vapor. Moreover, the absorption coefficients in the range of 40–115 cm $^{-1}$ were much higher for the butanone vapor.

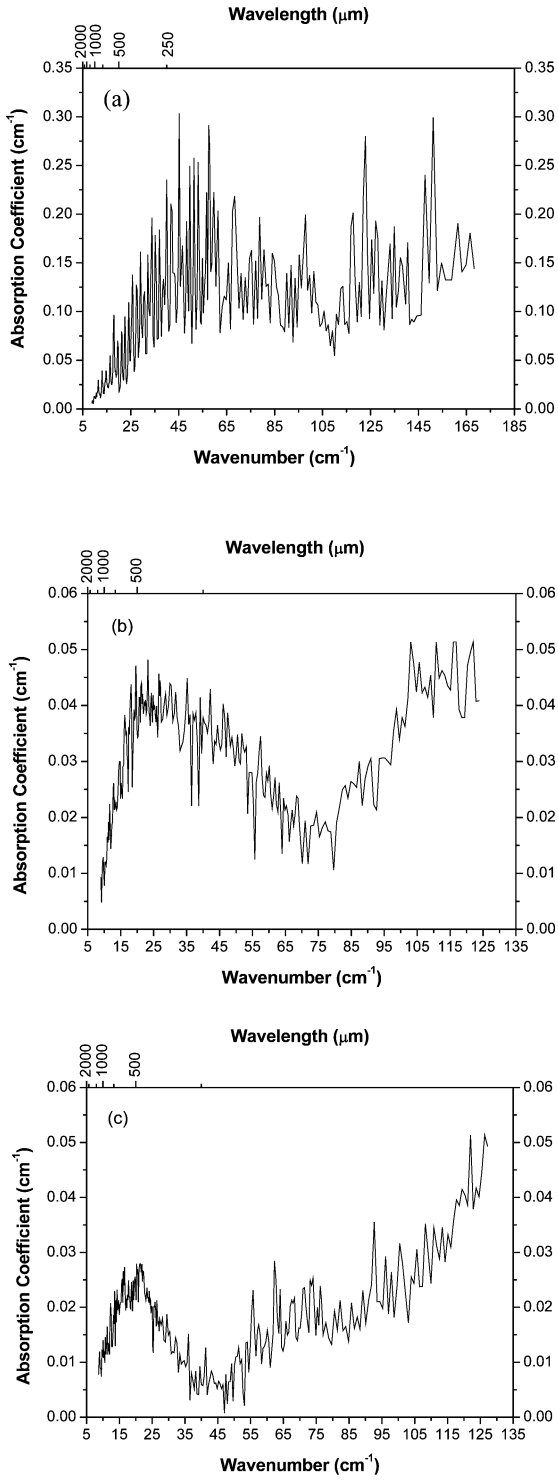

Fig. 21. Absorption coefficient versus wavenumber measured for (a) methanol vapor, (b) ethanol vapor, and (c) isopropanol vapor.

Finally, for the two members of the alkyl-halogenides homologues (i.e., dichloromethane vapor CH_2Cl_2 and chloroform

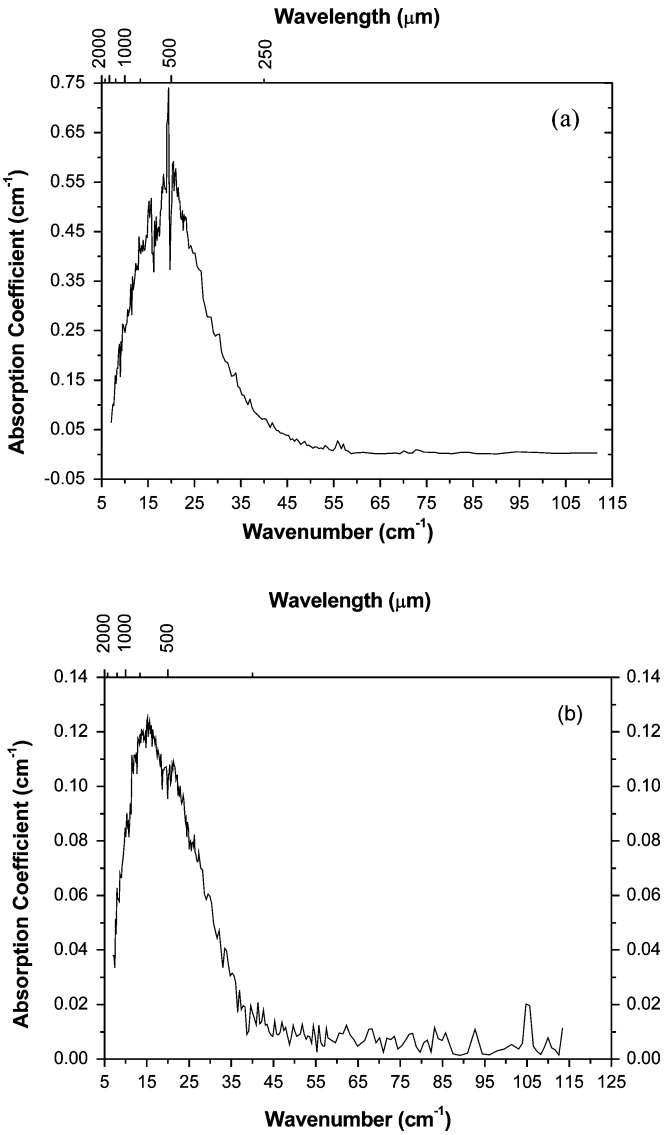

Fig. 22. Absorption coefficient versus wavenumber measured for (a) acetone vapor and (b) vapor of methyl ethyl ketone (butanone).

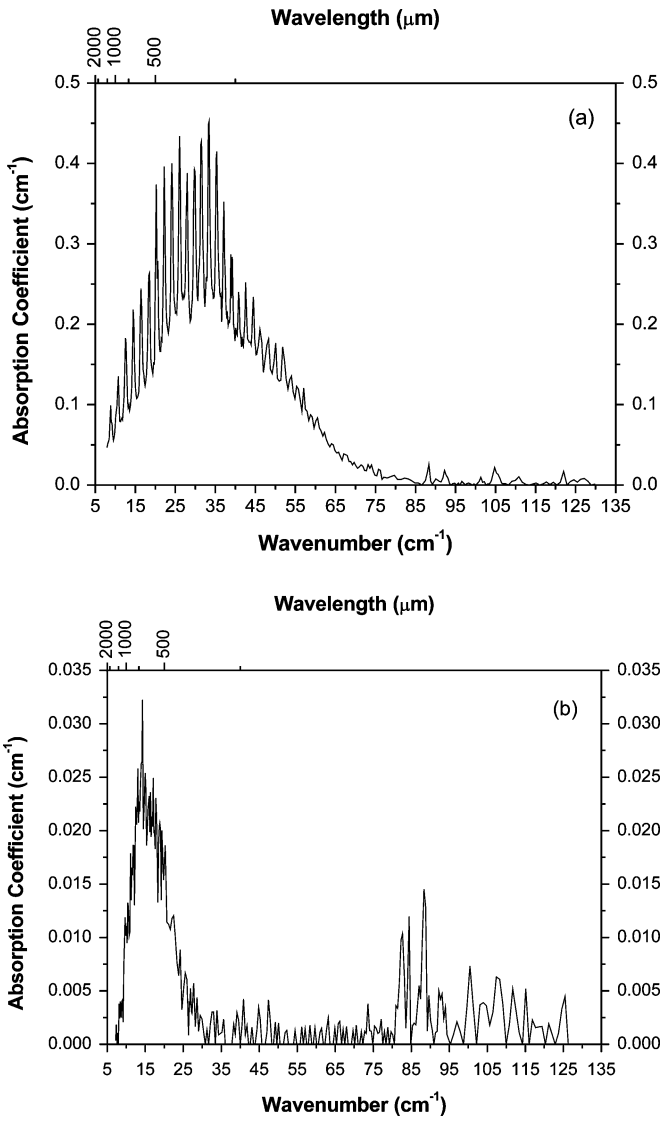

Fig. 23. Absorption coefficient versus wavenumber measured for (a) dichloromethane vapor and (b) chloroform vapor.

vapor $CHCl_3$) the absorption spectra were distinctly different; see Fig. 23. For the dichloromethane vapor, there were 29 sharp transition peaks in the range of 5–60 cm^{-1}. The absorption above 75 cm^{-1} was negligible. For the chloroform vapor, however, the absorption coefficients were much lower than those for the dichloromethane vapor. Furthermore, the absorption mainly occurred in the range of 7.4–30 cm^{-1}, although there was significant absorption in the range of 80–126 cm^{-1}. Therefore, just by replacing one hydrogen atom by one chlorine atom in each CH_2Cl_2 molecule, the absorption spectrum in the terahertz region was dramatically modified. This important comparison illustrates that the absorption spectra of chemicals in the terahertz domain are quite sensitive to their molecular structures.

Our terahertz source was also used to differentiate between isotopic variants. We have used ^{12} CO and ^{13} CO as an example [25]. These two isotopic variants are the most abundant among all the CO isotopic variants existing in nature. For a diatomic molecule, the frequency for each rotational transition line is given by [58]

$$\upsilon \approx 2B_0\,(J+1) \tag{9}$$

where B_0 is the rotational constant, and J is the rotational quantum number for the lower energy state of each transition. According to (9), the transition frequency linearly increases with J with $2B_0$ the slope of the increase. In the past, $^{12}C^{16}O$, $^{13}C^{16}O$, and $^{12}C^{18}O$ were measured by frequency-tuning the output of a photoconducting antenna pumped by two diode lasers [59]. However, only a single transition peak was measured for each isotopic variant due to a limited tuning range. Furthermore, the signal-to-noise ratio was limited by the output power and the absorption of gases, which can be low if fast scanning is necessary.

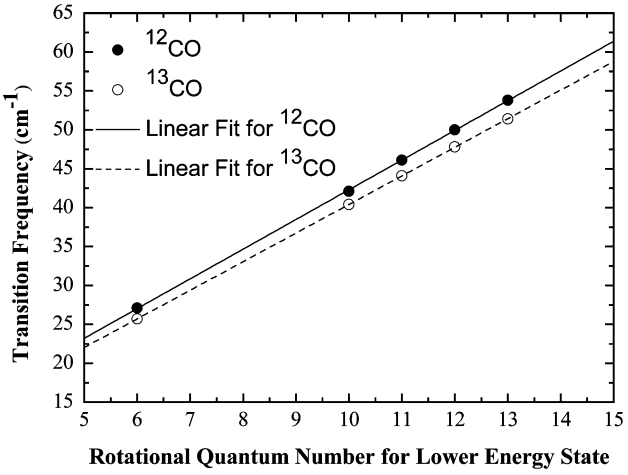

Fig. 24. Transition frequencies versus rotational quantum number of the lower energy state of each transition measured for ^{12}CO and ^{13}CO. Solid and dashed lines correspond to the least square fits to the measurements.

Two gas cells, each having a diameter of 9 mm and a length of 150 mm, were filled with the CO gases. These gas cells were made from quartz with fused silica being used as the input and output windows. The purities of ^{12}CO and ^{13}CO were 99.96% and 99%, respectively, and the pressure was kept at 600 torr for the two gas cells. By measuring the transmission spectra of the two gases, we identified five transition peaks for each isotopic variant and deduced the corresponding peak frequencies. We then used (9) to fit these measured transition frequencies; see Fig. 24. As a result, we obtained $2B_0 \approx 3.82$ cm^{-1} and 3.68 cm^{-1} for ^{12}CO and ^{13}CO, respectively. On the other hand, according to HITRAN database, $2B_0 \approx 3.84$ cm^{-1} and 3.67 cm^{-1} for ^{12}CO and ^{13}CO, respectively. Therefore, even though the linewidth of the terahertz source was measured to be around 0.36 cm^{-1} [60], the rotational constants measured by us deviated from the well-accepted values only by -0.01 cm^{-1} and 0.005 cm^{-1}, respectively. Since the rotational constants for ^{12}CO and ^{13}CO differ from each other by 0.07 cm^{-1}, our method for differentiating between the two CO isotopic variants is validated.

Tunable terahertz sources based on noncollinear TPO [11], [12] were used in the past to realize terahertz imaging [61], [62]. In [61], [62], the transmission spectra were used to either differentiate among different chemical species or discriminate against background objects. Indeed, in [61], the component spatial patterns of frequency-dependent absorption in palatinose and 5-aspirin were separated from frequency-independent components such as plastic, paper, and noise using known spectral curves. As a result, the component patterns of palatinose and 5-aspirin were readily extracted from the frequency-independent components in the frequency range of 1–2 terahertz. It was claimed that this method could be used to search for illegal drugs and device of bioterrorism concealed inside mails and packages. On the other hand, it was demonstrated in [62] that multispectral images of a target could be taken and analyzed in order to extract spatial patterns of chemicals such as aspirin, methamphetamine, and 3,4-methylenedioxy-N-methylamphetamine **(MDMA)**(i.e., ecstasy).

VII. Concluding Remarks

In conclusion, we have reviewed our most recent results on the efficient generation of the widely tunable monochromatic terahertz pulses. They were produced by mixing two coherent radiations in the near-infrared region in GaSe, $ZnGeP_2$, and GaP crystals, i.e., based on the phase-matched DFG. Among these three nonlinear optical crystals, a 47-mm-long GaSe crystal provides the widest tuning range, the highest peak power, and the highest corresponding conversion efficiency. On the other hand, since GaP is a cubic crystal, tuning within a wide frequency range was achieved without rotating the 20-mm-long GaP crystal. Based on power scaling, a shoebox-sized terahertz source for efficiently generating relatively high peak powers is feasible. We have observed backward terahertz DFG by using GaSe crystals and showed that it would be feasible for us to achieve backward parametric oscillation in GaSe and $ZnGeP_2$ crystals.

By using one of our widely tunable monochromatic terahertz sources, we have directly measured the absorption spectra of the three different families of the chemical vapors. Our results indicated that all these chemical vapors exhibited completely different absorption spectra, due to the transitions between the rotational energy states. We have also reviewed our most recent result following our demonstration that a tunable terahertz source was capable of differentiating between two CO isotopic variants. Therefore, it would be feasible for us to develop a terahertz spectrometer following our results to identify and to perhaps detect most chemicals in the vapor phase by measuring their distinct rotational transition frequencies in the terahertz region, similar to the process of identifying human beings based on their fingerprints. Such a spectrometer can be used to measure an absorption spectrum of a chemical species by frequency-tuning our monochromatic terahertz source rather than going through Fourier transform. Such an important application can be crucial to homeland security and national defense. We have also provided a brief overview on terahertz imaging implemented by using tunable narrowband terahertz sources.

Acknowledgment

The author would like to thank W. Shi, Y. B. Zotova, N. Fernelius, and H. Sun for making valuable contributions to some of the results reviewed in this paper.

References

[1] W. Gordy and R. L. Cook, *Microwave Molecular Spectra*, 3rd ed. New York: Wiley, 1984.

[2] R. A. McClatchey, R. W. Fenn, J. E. A. Selby, F. E. Volz, and J. S. Garing, *Optical properties of the atmosphereHandbook of Optics*, W. G. Driscoll ed. New York: McGraw-Hill, 1978.

[3] C. Tomasi, "Vertical mass loading of aerosol particles by sun-photometric measurements," in *Optical Remote Sensing of Air Pollution*, P. Camagni and S. Sandroni ed. New York: Elsevier, 1984.

[4] L. Xu, X.-C. Zhang, and D. H. Auston, "Terahertz beam generation by femtosecond optical pulses in electro-optic materials," *Appl. Phys. Lett.*, vol. 61, pp. 1784–1786, Oct. 1992.

[5] D. H. Auston, K. P. Cheung, and P. R. Smith, "Picosecond photoconducting Hertzian dipoles," *Appl. Phys. Lett.*, vol. 45, pp. 284–286, Aug. 1984.

[6] D. H. Auston, K. P. Cheung, J. A. Valdmanis, and D. A. Kleinman, "Cherenkov radiation from femtosecond optical pulses in electro-optic media," *Phys. Rev. Lett.*, vol. 53, pp. 1555–1558, Oct. 15, 1984.

[7] K. P. Cheung and D. H. Auston, "A novel technique for measuring far-infrared absorption and dispersion," *Infrared Phys.*, vol. 26, pp. 23–27, Jan. 1986.

[8] M. van Exter, C. Fattinger, and D. Grischkowsky, "Terahertz time-domain spectroscopy of water vapor," *Opt. Lett.*, vol. 14, pp. 1128–1130, Oct. 15, 1989.

[9] H.-B. Liu, Y. Chen, G. J. Bastiaans, and X.-C. Zhang, "Detection and identification of explosive RDX by terahertz diffuse reflection spectroscopy," *Opt. Exp.*, vol. 14, pp. 415–423, Jan. 2006.

[10] D. M. Mittleman, S. Hunnsche, L. Boivin, and M. C. Nuss, "T-ray tomography," *Opt. Lett.*, vol. 22, pp. 904–906, 1997.

[11] K. Kawase, M. Sato, T. Taniuchi, and H. Ito, "Coherent tunable terahertz-wave generation from $LiNbO_3$ with monolithic grating coupler," *Appl. Phys. Lett.*, vol. 68, pp. 2483–2485, Apr. 1996.

[12] K. Kawase, J. Shikata, and H. Ito, "Terahertz wave parametric source," *J. Phys. D: Appl. Phys.*, vol. 35, pp. R1–R14, 2002.

[13] W. Shi, Y. J. Ding, N. Fernelius, and K. L. Vodopyanov, "An efficient, tunable, and coherent 0.18—5.27 terahertz source based on GaSe crystal," *Opt. Lett.*, vol. 27, pp. 1454–1456, Aug. 2002.

[14] W. Shi and Y. J. Ding, "A monochromatic and high-power terahertz source tunable in the ranges of 2.7–38.4 μm and 58.2–3540 μm for variety of potential applications," *Appl. Phys. Lett.*, vol. 84, pp. 1635–1637, Mar. 2004.

[15] W. Shi and Y. J. Ding, "Tunable coherent radiation from terahertz to microwave by mixing two infrared frequencies in a 47-mm-long GaSe crystal," *Int. J. High Speed Electron. Syst.*, vol. 16, pp. 589–595, Jun. 2006.

[16] W. Shi and Y. J. Ding, "Coherent and widely-tunable terahertz and millimeter waves based on difference-frequency generation in GaSe and $ZnGeP_2$," *Opt. 2002, Opt. Photon. News*, p. 57, Dec. 2002.

[17] W. Shi and Y. J. Ding, "Continuously-tunable and coherent terahertz radiation by means of phase-matched difference-frequency generation in zinc germanium phosphide," *Appl. Phys. Lett.*, vol. 83, pp. 848–850, Aug. 2003.

[18] W. Shi, Y. J. Ding, and P. G. Schunemann, "Coherent terahertz waves based on difference-frequency generation in an annealed zinc-germanium phosphide crystal: Improvements on tuning ranges and peak powers," *Opt. Commun.*, vol. 233, pp. 183–189, Mar. 2004.

[19] W. Shi and Y. J. Ding, "Tunable terahertz waves generated by mixing two copropagating infrared beams in GaP," *Opt. Lett.*, vol. 30, pp. 1030–1032, May 2005.

[20] Y. J. Ding and W. Shi, "Efficient terahertz generation and frequency up-conversion in GaP crystals," *Solid State Electron.*, vol. 50, pp. 1128–1136, Jun. 2006.

[21] W. Shi, X. Mu, Y. J. Ding, and N. Fernelius, "Tunable and coherent nanosecond radiation in the range of 2.7—28.7 μm based on difference-frequency generation in gallium selenide," *Appl. Phys. Lett.*, vol. 80, pp. 3889–3891, May 2002.

[22] R. Köhler, A. Tredicucci, F. Beltram, H. E. Beere, E. H. Linfield, G. Davies, D. A. Ritchie, R. C. Lotti, and F. Rossi, "Terahertz semiconductor-heterostructure laser," *Nature*, vol. 417, pp. 156–159, May 2002.

[23] S. Kumar, B. S. Williams, Q. Hu, and J. L. Reno, "1.9 terahertz quantum-cascade lasers with one-well injector," *Appl. Phys. Lett.*, vol. 88, pp. 121123-1–121123-3, Mar. 2006.

[24] W. Shi and Y. J. Ding, "Chemical identification based on direct measurement of absorption spectrum by frequency-tuning monochromatic terahertz source," *Laser Phys. Lett.*, vol. 1, pp. 560–564, Nov. 2004.

[25] H. Sun, Y. J. Ding, and Y. B. Zotova, "Differentiation of CO isotopic variants by frequency-tuning a terahertz source," *Appl. Opt.*, vol. 46, no. 19, Jul. 2007.

[26] H. Sun, W. Shi, Z. Fu, Y. J. Ding, and Y. B. Zotova, *Bragg reflectors and 2-D photonic crystals in the terahertz region* in *Terahertz for Military and Security Applications III*, R. J. Hwu, D. L. Woolard, and M. J. Rosker, Eds. Bellingham, WA: SPIE, 2005, vol. 5790, pp. 104–115.

[27] E. D. Palik, *Handbook of Optical Constants of Solids III*. New York: Academic, 1998, p. 487 and p. 640.

[28] W. Shi, Y. J. Ding, N. Fernelius, and F. K. Hopkins, "Observation of difference-frequency generation by mixing of terahertz and near-infrared laser beams in a GaSe crystal," *Appl. Phys. Lett.*, vol. 88, pp. 101101-1–101101-3, Mar. 2006.

[29] V. G. Dmitriev, G. G. Gurzadyan, and D. N. Nikogosyan, *Handbook of Nonlinear Optical Crystals*. Berlin, Germany: Springer, 1999, p. 168.

[30] P. D. Mason, D. J. Jackson, and E. K. Gorton, "CO_2 laser frequency doubling in $ZnGeP_2$," *Opt. Commun.*, vol. 110, pp. 163–166, Aug. 1994.

[31] G. D. Boyd, T. J. Bridges, C. K. N. Patel, and E. Buehler, "Phase-matched submillimeter wave generation by difference-frequency mixing in $ZnGeP_2$," *Appl. Phys. Lett.*, vol. 21, pp. 553–555, Dec. 1972.

[32] G. C. Bhar, L. K. Samanta, D. K. Ghosh, and S. Das, "Tunable parametric $ZnGeP_2$ crystal oscillator," *Sov. J. Quantum Electron.*, vol. 17, pp. 860–861, Jul. 1987.

[33] D. E. Zelmon, E. A. Hanning, and P. G. Schunemann, "Refractive-index measurements and Sellmeier coefficients for zinc germanium phosphide form 2 to 9 μm with implications for phase matching in optical frequency-conversion devices," *J. Opt. Soc. Amer. B*, vol. 18, pp. 1307–1310, Sep. 2001.

[34] Y. J. Ding and I. B. Zotova, "Coherent and tunable terahertz oscillators, generators, and amplifiers," *J. Nonlinear Opt. Phys. Mater.*, vol. 11, pp. 75–97, Mar. 2002.

[35] Y. J. Ding and W. Shi, "Widely-tunable, monochromatic, and high-power terahertz sources and their applications," *J. Nonlinear Opt. Phys. Mater.*, vol. 12, pp. 557–585, Dec. 2003.

[36] W. L. Fraust and C. H. Henry, "Mixing of visible and near-resonance infrared light in GaP," *Phys. Rev. Lett.*, vol. 17, pp. 1265–1268, Dec. 1966.

[37] T. Tanabe, K. Suto, J. Nishizawa, K. Saito, and T. Kimura, "Tunable terahertz wave generation in the 3- to 7-terahertz region from GaP," *Appl. Phys. Lett.*, vol. 83, pp. 237–239, Jul. 2003.

[38] A. N. Pikhtin, V. T. Prokopenko, and A. D. Yas'kov, "Dispersion of the refractive index of light and permittivity of gallium phosphide," *Sov. Phys. Semicond.*, vol. 10, pp. 1224–1226, Nov. 1977.

[39] D. Zhang, L. A. Gordon, and Y. S. Wu, *et al.*, "16-μm infrared generation by difference-frequency mixing in diffusion-bonded-stacked GaAs," *Opt. Lett.*, vol. 23, pp. 1010–1012, Jul. 1998.

[40] W. Shi and Y. J. Ding, "Generation of backward terahertz waves in GaSe crystals," *Opt. Lett.*, vol. 30, pp. 1861–1863, Jul. 2005.

[41] Y. J. Ding and W. Shi, "From backward terahertz difference-frequency generation to parametric oscillation," *IEEE J. Sel. Topics Quantum Electron. Nonlinear Opt.*, vol. 12, no. 3, pp. 352–359, May/Jun. 2006.

[42] S. E. Harris, "Proposed backward wave oscillation in the infrared," *Appl. Phys. Lett.*, vol. 9, pp. 114–116, Aug. 1966.

[43] J. A. Giordmaine and R. C. Miller, "Tunable coherent parametric oscillation in $LiNbO_3$ at optical frequencies," *Phys. Rev. Lett.*, vol. 14, pp. 973–976, Jun. 1965.

[44] D. S. Chemla and E. Batifol, "Optical backward mixing in sodium nitrite," *Opt. Commun.*, vol. 11, pp. 57–61, May 1974.

[45] D. S. Chemla and E. Batifol, "Optical backward parametric fluorescence in sodium nitrite," *Appl. Phys. Lett.*, vol. 28, pp. 135–137, Feb. 1976.

[46] Y. J. Ding and J. B. Khurgin, "Generation of tunable coherent far-infrared waves based on backward optical parametric oscillation in gallium selenide," *J. Opt. Soc. Amer. B*, vol. 15, pp. 1567–1571, May 1998.

[47] Y. J. Ding and J. B. Khurgin, "Backward optical parametric oscillators and amplifiers," *IEEE J. Quantum Electron.*, vol. 32, no. 9, pp. 1574–1582, Sep. 1996.

[48] Y. J. Ding and J. B. Khurgin, "A new scheme for efficient generation of coherent and incoherent submillimeter to terahertz waves in periodically-poled lithium niobate," *Opt. Commun.*, vol. 148, pp. 105–109, Mar. 1998.

[49] I. B. Zotova and Y. J. Ding, "Spectral measurements of two-photon absorption coefficients for CdSe and GaSe crystals," *Appl. Opt.*, vol. 40, pp. 6654–6658, Dec. 20, 2001.

[50] R. W. Boyd, *Nonlinear Optics*, 2nd ed. Boston, MA: Academic, 2003, p. 93.

[51] K. L. Vodopyanov, "Parametric generation of tunable infrared radiation in $ZnGeP_2$ and GaSe pumped at 3 μm," *J. Opt. Soc. Amer. B*, vol. 10, pp. 1723–1729, Sep. 1993.

[52] G. B. Abdullaev, K. R. Allakhverdiev, and M. E. Karasev, *et al.*, "Efficient generation of the second harmonic of CO_2 laser radiation in a GaSe crystal," *Kvantovaya Elektronika, Mosk*, vol. 16, pp. 757–63, 1989.

[53] K. L. Vodopyanov, Y. A. Andreev, and G. C. Bhar, "Parametric superluminescence in a $ZnGeP_2$ crystal with temperature tuning and pumping by an erbium laser," *Kvantovaya Elektronika, Mosk*, vol. 20, pp. 879–882, Sep. 1993.

[54] F. C. De Lucia, "Science and technology in the submillimeter region," *Opt. Photon. News*, vol. 14, pp. 44–54, Aug. 2003.

[55] A. Gambi, R. Visinoni, S. Giorgianni, and A. De Lorenzi, "High-resolution FTIR spectrum of the ν_5 band of 1,1-difluoroethylene around 550 cm^{-1}," *J. Mol. Spectrosc.*, vol. 145, pp. 270–277, Feb. 1991.

[56] F. R. Peterson, K. M. Evenson, D. A. Jennings, and A. Scalabrin, "Far infrared frequency synthesis with stabilized CO_2 lasers: Accurate measurements of the water vapor and methyl alcohol laser frequencies," *IEEE J. Quantum Electron.*, vol. QE-11, no. 10, pp. 838–843, Oct. 1975.

[57] N. Ioli, A. Moretti, and F. Strumia, "High efficiency cw far infrared laser at 119 μm and 127 μm," *Appl. Phys. B*, vol. 48, pp. 305–309, Apr. 1989.

[58] G. Klapper, F. Lewen, R. Gendriesch, S. P. Belov, and G. Winnewisser, "Sub-Doppler measurements of rotational spectrum of $^{13}C^{16}O$," *J. Mol. Spectrosc.*, vol. 201, pp. 124–127, May 2000.

[59] S. Matsuura, M. Tani, H. Abe, K. Sakai, H. Ozeki, and S. Saito, "High-resolution terahertz spectroscopy by a compact radiation source based on photomixing with diode lasers in a photoconducting antenna," *J. Mol. Spectrosc.*, vol. 187, pp. 97–101, Jan. 1998.

[60] Y. J. Ding and W. Shi, "Phase-matched frequency mixing of terahertz and near-infrared laser pulses in a $ZnGeP_2$crystal," *Opt. Exp.*, vol. 14, pp. 8311–8316, Sep. 4, 2006.

[61] Y. Watanabe, K. Kawase, T. Ikari, H. Ito, Y. Ishikawa, and H. Minamide, "Spatial pattern separation of chemicals and frequency-independent components by terahertz spectroscopic imaging," *Appl. Opt.*, vol. 42, pp. 5744–5748, Oct. 2003.

[62] K. Kawase, Y. Ogawa, H. Minamide, and H. Ito, "Terahertz parametric sources and imaging applications," *Semicond. Sci. Technol.*, vol. 20, pp. S258–S265, Jul. 2005.

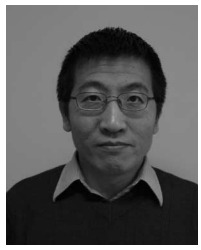

Yujie J. Ding (SM'04–SM'05) received the B.S. degree in electronic sciences from Jilin University, Changchun, China, in 1984, the M.S.E.E. degree from Purdue University, West Lafayette, IN, in 1987, and the Ph.D. degree in electrical engineering from The Johns Hopkins University, Baltimore, MD, in 1990.

During 1990–1992, he was appointed as a Postdoctoral Fellow and later as an Associate Research Scientist at The Johns Hopkins University. From 1992 to 1999, he was an Assistant, and then an Associate Professor of physics at Bowling Green State University, Bowling Green, KY. During 1999–2002, he was an Associate Professor of physics at the University of Arkansas. In 2002, he joined Lehigh University, Bethlehem, PA, where he is currently a Professor of electrical and computer engineering. He has published more than 100 refereed journal articles in optoelectronics, nonlinear optics, and quantum electronics. His current research interests include terahertz generation, amplification and detection, nanostructures and nanodevices, and their applications.

Dr. Ding is the recipient of the Class of 1961 Professorship from Lehigh University, Bethlehem, PA, in 2003 and the Outstanding Young Scholar Award from Bowling Green State University in 1996.